INTERNATIONAL SOCIETY FOR
SOIL MECHANICS AND
GEOTECHNICAL ENGINEERING

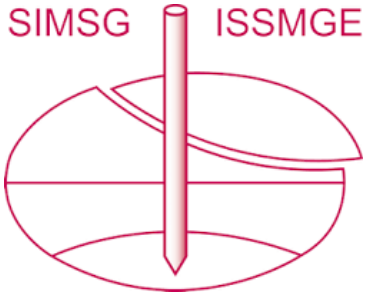

This paper was downloaded from the Online Library of the International Society for Soil Mechanics and Geotechnical Engineering (ISSMGE). The library is available here:

https://www.issmge.org/publications/online-library

This is an open-access database that archives thousands of papers published under the Auspices of the ISSMGE and maintained by the Innovation and Development Committee of ISSMGE.

Seismic behaviour of unsaturated embankment after rainfall

R. Uzuoka
Disaster Prevention Research Institute, Kyoto University, Uji, Japan

D. Hizen & Y. Nakai
Department of Civil and Environmental Engineering, Tokushima University, Tokushima, Japan

T. Matsumaru
Railway Technical Research Institute, Kokubunji, Japan

K-H. Yang
Department of Civil Engineering, National Taiwan University, Taipei, Taiwan

ABSTRACT: This study performed numerical analyses of seismic behaviour of an unsaturated embankment with various soil properties after various rainfall histories in order to understand the effect of rainfall histories on seismic behaviour of the unsaturated embankment. Soil-water-air coupled analysis code was used to simulate the seismic behaviour of the unsaturated embankment after various rainfall. The equations governing the dynamic deformation of unsaturated soil were derived based on porous media theory and constitutive model. The effective stress-strain relation was a simplified elasto-plastic model based on a nonlinear hardening rule and a non-associated flow rule. The water retention curve was assumed as a tangential model considering hysteresis. The numerical results showed that seismic failure modes after earthquake were significantly affected by the soil properties of embankment and the rainfall histories. For example, in the cases of clay embankment, the high saturation portion was concentrated on the embankment top and along the slope after the delayed rainfall pattern, and the earthquake-induced deviatoric strain became large along the embankment slope.

1 INTRODUCTION

Some Asian countries share a similar natural environment and face the same threats from natural disasters such as earthquake, typhoon, heavy rainfall, flood, landslide, debris flow and so on. What makes a bad situation even worse is that, these natural disasters very often did not come alone, which is known as combined disasters. For example, a heavy rain and an earthquake likely occur sequentially in a relatively short period. However, effect of rainfall histories on seismic behaviour of embankment has not been studied sufficiently. A few case studies (Faris & Wang 2013; Wang & Liu 2014) discussed combined effect of rainfall and earthquake on landslides, and an experimental study (Tiwari et al. 2013) examined slope stability after rainfall with shaking table tests.

In this study, numerical analyses of seismic behaviour of an unsaturated embankment was performed with various soil properties after various rainfall histories in order to understand the effect of rainfall histories on seismic behaviour of embankment. Soil-water-air coupled analysis code was used to simulate the seismic behaviour of unsaturated embankment after various rainfall. The equations governing the dynamic deformation of unsaturated soil were derived based on porous media theory and constitutive model. The effective stress-strain relation was a simplified elasto-plastic model based on nonlinear hardening rule and non-associated flow rule. The water retention curve was assumed as a tangential model considering hysteresis. The effect of rainfall histories on seismic behaviour of the unsaturated embankment based on the numerical results is discussed in this study.

2 NUMERICAL METHODS

2.1 *Governing equations*

Soil-water-air coupled analysis code was used (Uzuoka & Borja 2012; Matsumaru & Uzuoka 2014; Matsumaru & Uzuoka 2016) to simulate the seismic behaviour of unsaturated embankment after various rainfall. The equations governing the dynamic deformation of unsaturated soil are derived based on porous media theory and constitutive model. The governing equations consist of the momentum balance equations of the overall three-phase material, and the mass and momentum balance equations (continuity equations) of the pore water and air derived with the following assumptions- 1) The soil particle is incompressible; 2) The mass exchange among phases is neglected; 3) The material time derivative of relative velocities and advection terms of pore fluids to the soil skeleton are neglected; 4) An isothermal condition are assumed. The momentum balance equations of the overall three-phase material are derived as-

$$\rho \mathbf{a}^s = \mathrm{div}\left\{\boldsymbol{\sigma}' - (s^w p^w + s^a p^a)\mathbf{I}\right\} + \rho \mathbf{b} \tag{1}$$

where ρ is the overall density of three-phase material; $\boldsymbol{a}^s$ is the acceleration vector of solid phase; $\boldsymbol{\sigma}'$ is the Cauchy effective stress tensor; s^{w} is the degree of water saturation; s^{a} is the degree of air saturation; p^{w} is the pore water pressure; p^{a} is the pore air pressure; $\mathbf{I}$ is the unit tensor and $\boldsymbol{b}$ is the body force vector. The stress and strain are positive in tension and the pore fluid pressures are positive in compression. The Cauchy effective stress tensor is so called average skeleton stress (Gallipoli et al. 2003) which is equivalent to Bishop's effective stress with s^{w} in place of parameter χ. The mass and momentum balance equations of the pore water and air are derived as-

$$\begin{aligned}&\left(\frac{ns^w\rho^{wR}}{K^w} - n\rho^{wR}c\right)\frac{D^s p^w}{Dt} + n\rho^{wR}c\frac{D^s p^a}{Dt}\\ &+s^w\rho^{wR}\,\mathrm{div}\,\mathbf{v}^s\\ &+\mathrm{div}\left\{\frac{k^{ws}}{g}\left(-\mathrm{grad}\,p^w + \rho^{wR}\mathbf{b} - \rho^{wR}\mathbf{a}^s\right)\right\} = 0\end{aligned} \tag{2}$$

where n is the porosity; ρ^{wR} is the intrinsic densities of pore water; K^{w} is the bulk modulus of pore water; c is the specific water capacity; $\boldsymbol{v}^{\mathrm{s}}$ is the velocity vector of soil skeleton; k^{ws} is the permeability coefficient of water; g is the gravity acceleration; $\mathrm{D}^{\mathrm{s}}\square/\mathrm{D}t$ is the material time derivative with respect to soil skeleton. Similarly, the mass and momentum balance equation of the pore air with respect to the current configuration is derived as-

$$\begin{aligned}&\left(\frac{ns^a}{\Theta\overline{R}} - n\rho^{aR}c\right)\frac{D^s p^a}{Dt} + n\rho^{aR}c\frac{D^s p^w}{Dt}\\ &+s^a\rho^{aR}\,\mathrm{div}\,\mathbf{v}^s\\ &+\mathrm{div}\left\{\frac{k^{as}}{g}\left(-\mathrm{grad}\,p^a + \rho^{aR}\mathbf{b} - \rho^{aR}\mathbf{a}^s\right)\right\} = 0\end{aligned} \tag{3}$$

where Θ is the absolute temperature; $\overline{R}$ is the specific gas constant of air; ρ^{aR} is the intrinsic densities of pore air; k^{as} is the permeability coefficient of air. This simplified formulation is called u-p^{w}-p^{a} formulation. Although the governing equations were derived in the regime of finite strain, infinitesimal strain was assumed in the following study for simplicity.

2.2 *Constitutive equation for skeleton stress*

A simplified elasto-plastic constitutive equation for skeleton stress was used in this study. Assuming that, plastic deformation occurs only when the deviatoric stress ratio changes, the yield function was assumed as-

$$f = \sqrt{\frac{3}{2}}\left\|\boldsymbol{\eta} - \boldsymbol{\alpha}\right\| - k = \sqrt{\frac{3}{2}}\left\|\mathbf{s}/p' - \boldsymbol{\alpha}\right\| - k = 0 \tag{4}$$

where p' is the mean skeleton stress; $\boldsymbol{s}$ is the deviatoric stress tensor; k is the material parameter which defines the elastic region; $\boldsymbol{\alpha}$ is the kinematic hardening parameter (back stress) and its nonlinear evolution rule (Armstrong & Frederick 1966) was assumed as-

$$\dot{\boldsymbol{\alpha}} = a\left(\frac{2}{3}b\dot{\boldsymbol{\varepsilon}}^p - \boldsymbol{\alpha}\dot{\varepsilon}_d^p\right),\quad \dot{\varepsilon}_d^p = \sqrt{\frac{2}{3}}\left\|\dot{\boldsymbol{\varepsilon}}^p\right\| \tag{5}$$

where a, b are the material parameters; $\dot{\boldsymbol{\varepsilon}}^p$ is the plastic deviatoric strain rate tensor. The material parameter a was assumed to be dependent on the value of the equivalent plastic strain $\dot{\varepsilon}_d^{p(n)}$ which is reset when the direction of loading changes,

$$a = a_0 - \frac{a_0 - a_1}{1 + (a_0 - a_1)\exp\left(-C_f\dot{\varepsilon}_d^{p(n)}\right)} \tag{6}$$

where a_0 is the initial value of the material parameter a; a_1 is the lower limit value of a and C_{f} is the parameter which controls the amount of the reduction of a. In order to describe plastic strain rate more precisely, the non-associated flow rule was adopted as-

$$\dot{\boldsymbol{\varepsilon}}^p = \dot{\gamma}\frac{\partial g}{\partial \mathbf{s}},\quad \dot{\varepsilon}_v^p = D\dot{\gamma}\frac{\partial g}{\partial p'} \tag{7}$$

where $\dot{\gamma}$ is the hardening coefficient; g is the plastic potential function $\dot{\varepsilon}_v^p$ and D is the coefficient of dilatancy. In order to consider the suction effect on the plastic volumetric strain rate of unsaturated soil, the suction-dependent dilatancy coefficient was used as-

$$\begin{aligned}&D = D_1 + (D_0 - D_1)\exp\left(-p^c / p^c_{ref}\right) && (p^c > 0)\\ &D = D_0 && (p^c \le 0)\end{aligned} \tag{8}$$

where D_0 is the initial value of the coefficient of dilatancy D; D_1 is the lower limit value of D and p^c_{ref} is the parameter which controls the amount of the reduction of D with the suction $p^c (= p^a - p^w)$. The Equation (8) describes that the plastic volumetric strain becomes small with large suction. With non-associated flow rule, the plastic potential function was assumed as-

$$g = \sqrt{\frac{3}{2}}\left\|\boldsymbol{\eta} - \boldsymbol{\alpha}\right\| + M_m \ln\left(p'/p'_a\right) = 0 \tag{9}$$

where M_{m} is the material parameter which defines the critical state ratio; p'_{a} is p' when $\left\|\boldsymbol{\eta} - \boldsymbol{\alpha}\right\| = 0$. Finally, stress-dependent elastic module were assumed as-

$$K^e = -K^* p' \quad G^e = -G^* p' \tag{10}$$

where K^e is the elastic bulk modulus; G^e is the elastic shear modulus; K^* and G^* are the dimensionless elastic module respectively.

2.3 *Water retention curve*

The specific water capacity is defined as the tangent of the water retention curve (WRC). The main curves of WRC were assumed as-

$$\begin{aligned} s^{\mathrm{w}} &= (s_{\mathrm{s}}^{\mathrm{w}} - s_{\mathrm{r}}^{\mathrm{w}}) s_{\mathrm{e}}^{\mathrm{w}} + s_{\mathrm{r}}^{\mathrm{w}} \\ s_{\mathrm{ed}}^{\mathrm{w}} &= \left\{1 + (p^{\mathrm{c}} / a_d)^{m_{\mathrm{d}}}\right\}^{-n_{\mathrm{d}}} \quad \text{(drying)} \\ s_{\mathrm{ew}}^{\mathrm{w}} &= \left\{1 + (p^{\mathrm{c}} / a_w)^{m_{\mathrm{w}}}\right\}^{-n_{\mathrm{w}}} \quad \text{(wetting)} \end{aligned} \tag{11}$$

where $s^{\mathrm{w}}_{\mathrm{s}}$ is the saturated (maximum) degree of saturation; $s^{\mathrm{w}}_{\mathrm{r}}$ is the residual (minimum) degree of saturation and $s^{\mathrm{w}}_{\mathrm{e}}$ is the effective water saturation. The subscripts 'd' and 'w' of $s^{\mathrm{w}}_{\mathrm{e}}$ stand for drying and wetting respectively. The relationship between $s^{\mathrm{w}}_{\mathrm{e}}$ and suction p^{c} was assumed as the van Genuchten (VG) model (van Genuchten 1980) with the material parameters a_{d}, n_{d} and m_{d} (main drying) and a_{w}, n_{w} and m_{w} (main wetting). In addition, the scanning curves of WRC were described with a tangential model (Zhou et al. 2012) between main drying and wetting curves defined with the above VG model,

$$\begin{aligned} \frac{\partial s_{\mathrm{es}}^{\mathrm{w}}}{\partial p^{\mathrm{c}}} &= \left(\frac{p_d^c}{p^{\mathrm{c}}}\right)^{-b} \frac{\partial s_{\mathrm{ed}}^{\mathrm{w}}}{\partial p^{\mathrm{c}}} \quad \text{(drying)} \\ \frac{\partial s_{\mathrm{es}}^{\mathrm{w}}}{\partial p^{\mathrm{c}}} &= \left(\frac{p_w^c}{p^{\mathrm{c}}}\right)^{b} \frac{\partial s_{\mathrm{ew}}^{\mathrm{w}}}{\partial p^{\mathrm{c}}} \quad \text{(wetting)} \end{aligned} \tag{12}$$

where p_d^c and p_w^c are the suction corresponding to the drying and wetting boundaries respectively at the same effective degree of saturation as the current point and the subscript 's' stands for scanning. The permeability coefficient of water and air were assumed to be dependent on the effective water saturation as-

$$\begin{aligned} k^{\mathrm{ws}} &= k_{\mathrm{s}}^{\mathrm{w}} (s_{\mathrm{e}}^{\mathrm{w}})^{\xi_{\mathrm{vg}}} \\ k^{\mathrm{as}} &= k_{\mathrm{s}}^{\mathrm{a}} (1 - s_{\mathrm{e}}^{\mathrm{w}})^{\eta_{\mathrm{vg}}} \end{aligned} \tag{13}$$

where $k^{\mathrm{w}}_{\mathrm{s}}$ is the saturated (maximum) coefficient of water permeability; $k^{\mathrm{a}}_{\mathrm{s}}$ is the dry (maximum) coefficient of air permeability; ξ_{vg} and η_{vg} are the material parameters.

2.4 *Finite element formulation and time integration*

Weak forms of the Equations (1) - (3) were implemented in a finite element formulation. Newmark implicit scheme was used for time integration. The primary variables are the second-order material time derivative of displacement of soil skeleton $\ddot{\mathbf{a}}^s$; pore water pressure $\ddot{p}^w$ and pore air pressure $\ddot{p}^a$. The weak forms are linearized and solved by Newton-Raphson method iteratively at each time step. The linearized forms of the weak forms were derived as-

$$\begin{aligned} D\delta w^s[\Delta \mathbf{a}^s] + D\delta w^s[\Delta \ddot{p}^w] + D\delta w^s[\Delta \ddot{p}^a] &= -\delta w^s_{(k)} \\ D\delta w^w[\Delta \mathbf{a}^s] + D\delta w^w[\Delta \ddot{p}^w] + D\delta w^w[\Delta \ddot{p}^a] &= -\delta w^w_{(k)} \\ D\delta w^a[\Delta \mathbf{a}^s] + D\delta w^a[\Delta \ddot{p}^w] + D\delta w^a[\Delta \ddot{p}^a] &= -\delta w^a_{(k)} \end{aligned} \tag{14}$$

where δw^{s}, δw^{w} and δw^{a} are the weak forms of the Equations (1), (2) and (3) respectively; $D\delta w^{\mathrm{s}}[\Delta \mathbf{a}^{\mathrm{s}}]$ is directional derivative of δw^{s} with respect to $\Delta \mathbf{a}^{\mathrm{s}}$; the $\delta w^{\mathrm{s}}_{(k)}$ is the residual at the iteration step of (k). The iteration was continued until the norm of the residual vectors became less than the convergence tolerance of 1.0×10^{-8}. In the finite element formulation, Galerkin method and isoparametric 8-node elements were used. The soil skeleton displacement and the fluid pressures were approximated at 8 nodes and 4 nodes respectively to satisfy the discrete LBB conditions for the locally undrained case at infinitesimal deformation.

2.5 *Implicit stress integration*

Implicit stress integration and consistent tangent modulus at infinitesimal strain (e.g. Simo & Taylor 1985) were used to achieve the convergence of global iteration of (14). The return mapping algorithm in stress space was used as-

$$\mathbf{r}_1 = \boldsymbol{\sigma}' - \boldsymbol{\sigma}'^{(\mathrm{tr})} + \Delta\gamma \mathbf{c}^e \frac{\partial g}{\partial \boldsymbol{\sigma}'}, \mathbf{r}_2 = \boldsymbol{\alpha} - \boldsymbol{\alpha}_n + \Delta\boldsymbol{\alpha}, r_3 = f \tag{15}$$

where $\boldsymbol{\sigma}'^{(\mathrm{tr})}$ is the trial skeleton stress for a given strain increment at the global iteration step; $\Delta\gamma$ is the plastic multiplier; $\boldsymbol{c}^{\mathrm{e}}$ is the elastic tensor; $\boldsymbol{\alpha}_{\mathrm{n}}$ is $\boldsymbol{\alpha}$ at the previous time step; $\Delta\boldsymbol{\alpha}$ is the increment of $\boldsymbol{\alpha}$. Until the norm of left-handed residual vector $\boldsymbol{r}$ of (15) became less than the convergence tolerance of 1.0×10^{-10}, the nonlinear equations were solved iteratively by Newton-Raphson method with respect to $\boldsymbol{\sigma}'$, $\boldsymbol{\alpha}$ and $\Delta\gamma$. The skeleton stress and back stress for a given strain increment at the global iteration step were obtained by local iteration of (15) at each stress integration point. The consistent tangent modulus was obtained as-

$$\mathbf{c}^{ep} = \frac{\partial \boldsymbol{\sigma}'}{\partial \boldsymbol{\varepsilon}^{e(tr)}} = \frac{\partial \boldsymbol{\sigma}'}{\partial \boldsymbol{\varepsilon}} \tag{16}$$

where $\boldsymbol{c}^{\mathrm{ep}}$ is the elasto-plastic tensor; $\boldsymbol{\varepsilon}^{\mathrm{e(tr)}}$ is the trial elastic strain (given strain). The differentiation in (16) was carried out at each converged stress derived from the local iteration of (15).

3 NUMERICAL CONDITIONS

Figure 1 shows the finite element model of an unsaturated embankment with a single material. Two kinds of materials of embankment were used; a fine

sand and a clay. The material parameters of fine sand and clay were referred to Matsumaru and Uzuoka (2014) as well as Matsumaru and Uzuoka (2016), respectively. Only the material parameters for the hysteresis, VG model was changed in this study as shown in Table 1 and Figure 2.

Before a seismic analysis, the static self-weight analysis and seepage analysis were performed in order to determine the initial stress and moisture conditions after rainfall. At the bottom of embankment, the soil displacement was fixed in all directions and no flux of water and air were assumed. Figure 3 shows two different rainfall histories with the same total amount of rainfall. In Case (a), heavy rain comes at the beginning, and it gradually decreases. In Case (b), rainfall gradually increases, and it reaches to the peak at the end. The time increment was 10 seconds in the seepage analyses in which the inertia terms were neglected.

In the seismic analysis, the input acceleration in Figure 4 is applied at the bottom. This acceleration was the modified wave observed during 2004 Niigata-ken Chuetsu earthquake (Matsumaru & Uzuoka 2016). The coefficients in Newmark implicit time integration were 0.6 and 0.3025. The time increment was 0.002 seconds in the seismic analysis. Rayleigh damping with the factor of 0.002 was used for the initial stiffness.

4 NUMERICAL RESULTS AND DISCUSSION

Figures 5 shows the distributions of water saturation in the embankment during the rainfall as shown in Figure 3. In the case of fine sand, the high saturation portion was seen near the bottom in both rainfall histories. In the case of clay, the high saturation portion was concentrated near the toe of slope with the rainfall history of Case (a), while on the embankment top and along the slope with the rainfall history of Case (b). The clay embankment was clearly affected by the rainfall histories due to the low permeability.

Figure 6 shows the equivalent strain distributions during the seismic response analysis without rainfall. In the cases without rainfall before the shaking, the large equivalent strain portion was concentrated near the shoulder of both fine sand and clay embankments.

Figure 7 shows the equivalent strain distributions during the seismic response analysis after rainfall. In the cases with rainfall before the shaking, the higher equivalent strain portion was observed than the cases without rainfall before shaking. In addition, the large equivalent strain was concentrated near the toe of embankment slope in most cases, while the large strain portion was concentrated near the shoulder of both fine sand and clay embankments without rainfall. In the cases of fine sand embankment, the large equivalent strain occurred near the toe of embank-

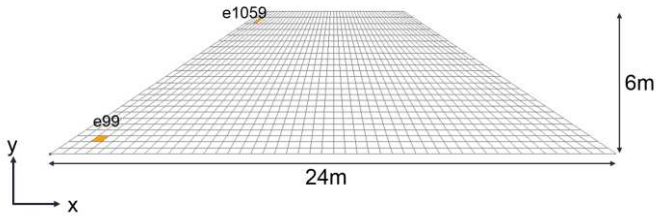

Figure 1. Finite element model of an embankment.

Table 1. Material parameters of hysteresis VG model

For fine sand embankment	
Main drying curve, a_d, m_d, n_d	8.0, 3.0, 1.0
Main wetting curve, a_w, m_w, n_w	2.0, 3.0, 1.0
Scanning curve, b	3.0
For clay embankment	
Main drying curve, a_d, m_d, n_d	8.0, 2.0, 0.7
Main wetting curve, a_w, m_w, n_w	2.0, 2.0, 0.7
Scanning curve, b	3.0

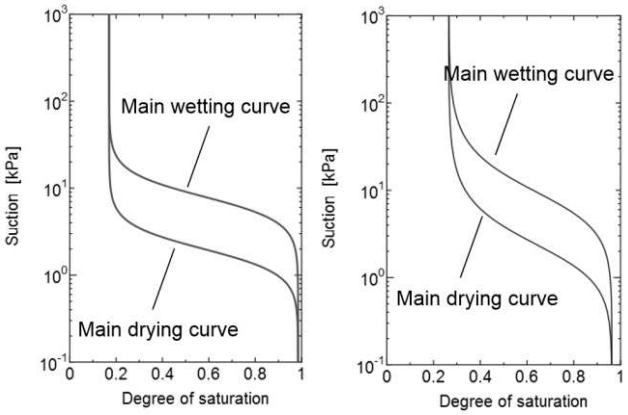

Figure 2. WRC of embankment (left: fine sand; right: clay).

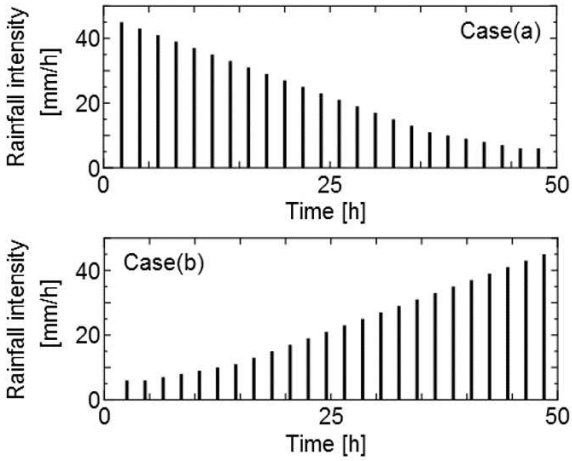

Figure 3. Rainfall histories.

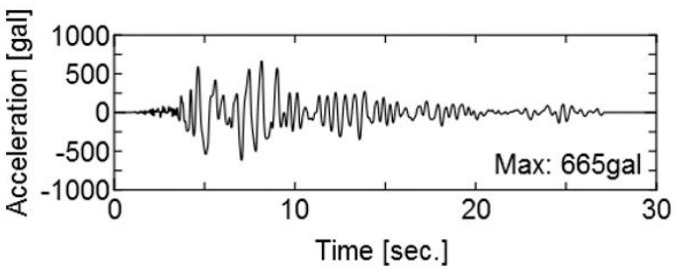

Figure 4. Input acceleration time history (Matsumaru & Uzuoka 2016).

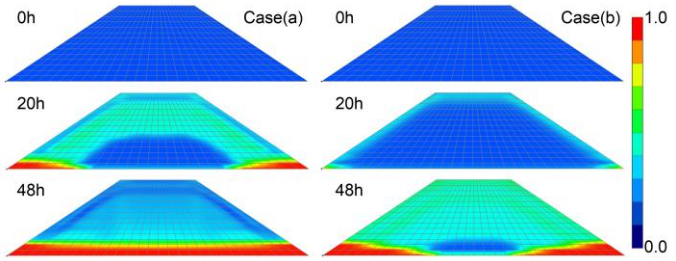

(a) Fine sand embankment

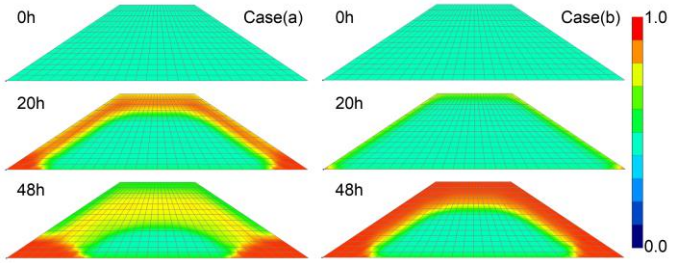

(b) Clay embankment

Figure 5. Distributions of degree of saturation after rainfall.

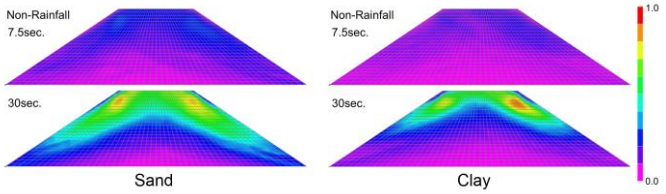

Figure 6. Distributions of equivalent strain during and after shaking (without rainfall histories).

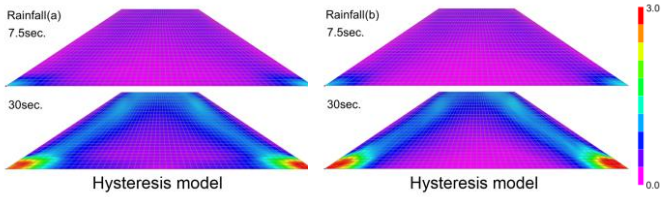

(a) Fine sand embankment

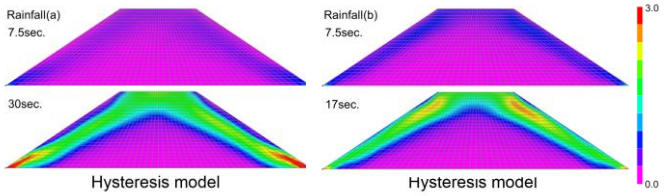

(b) Clay embankment

Figure 7. Distributions of equivalent strain during and after shaking (with rainfall histories).

ment slope in both cases with different rainfall histories. The effect of rainfall histories on the seismic behaviour is not significant in the cases of fine sand embankment because the distributions of degree of saturation were not largely different as shown in Figure 5 (a). In the cases of clay embankment, the large equivalent strain occurred near the toe of embankment in Case (a), while the equivalent strain along the slope was large in Case (b). These results correspond to the different distributions of water saturation after rainfall as shown in Figure 5 (b). It is suggested that the rainfall history causes different failure modes after earthquake in the cases of low permeable embankment. We need further investigations about the effect of other factors such as soil type, configuration of embankment, and input motions.

5 CONCLUSIONS

We performed numerical analyses of seismic behaviour of an unsaturated embankment with various soil properties after various rainfall histories in order to understand the effect of rainfall histories on seismic behaviour of embankment. We used soil-water-air coupled analysis code to simulate the seismic behaviour of unsaturated embankment after various rainfall. The numerical results showed that seismic failure modes after earthquake were significantly affected by the soil properties of embankment and the rainfall histories. For example, in the cases of clay embankment, the high saturation portion was concentrated on the embankment top and along the slope with the delayed rainfall pattern, and earthquake induced equivalent strain became large along the embankment slope.

6 ACKNOWLEDGEMENTS

This study was financially supported by the Collaboration Program by and between Tokushima University and National Taiwan University of Science and Technology.

7 REFERENCES

Armstrong, P.J. & Frederick, C.O. 1966. A mathematical representation of the multiaxial Bauschinger effect. C.E.G.B. Report RD/B/N731, Berkeley Nuclear Laboratories, Berkeley, UK.

Faris, F. & Wang, F. 2013. Investigation on failure mechanism of earthquake induced landslide during rainfall: a case study of Yandikat landslide, West Sumatra, Indonesia. *International Journal of Landslide and Environment* 1(1): 15-16.

Gallipoli, D., Gens, A., Sharma, R. & Vaunat, J. 2003. An elasto-plastic model for unsaturated soil incorporating the effects of suction and degree of saturation on mechanical behaviour. *Geotechnique* 53(1): 123-135.

Van Genuchten, M.T. 1980. A closed-form equation for predicting the hydraulic conductivity of unsaturated soils. *Soil Sci. Soc. Am. J.* 44: 892-898.

Matsumaru, T. & Uzuoka, R. 2014. Two-phase and three-phase coupled analysis of embankment affected by seepage water and earthquake. *Computer Methods and Recent Advances in Geomechanics - Proceedings of IACMAG*: 1379-1384.

Matsumaru, T. & Uzuoka, R. 2016. Three-phase seepage-deformation coupled analysis about unsaturated embankment damaged by earthquake. *International Journal of Geomechanics* 16(5): C4016006-1-12.

Simo, J.C. & Taylor, R.L. 1985. Consistent tangent operators for rate-independent elasto-plasticity. *Computer Methods in Applied Mechanics and Engineering* 48: 101-118.

Tiwari, B., Lewis, A. & Ferrar, E. 2013. Experimental simulation of rainfall and seismic effects to trigger slope failures. *Geo-Congress*: 448-451.

Uzuoka, R. & Borja, R.I. 2012. Dynamics of unsaturated poro-elastic solids at finite strain. *International Journal for Numerical and Analytical Methods in Geomechanics* 36: 1535-1573.

Wang, J. & Liu, X. 2014. A preliminary study of joint effect of earthquake disturbing and rainfall on Yiliang landslide. *Advances in Soil Dynamics and Foundation Engineering GSP* 240: 563-571.

Zhou, A.N., Sheng, D., Sloan, S.W. & Gens, A. 2012. Interpretation of unsaturated soil behaviour in the stress - Saturation space, I: Volume change and water retention behaviour. *Computers and Geotechnics* 43: 178-187.